Two-electron photoionization of ground-state lithium

A. S. Kheifets*
Research School of Physical Sciences, The Australian National University, Canberra, Australian Capital Territory 0200, Australia

D. V. Fursa and I. Bray
ARC Centre for Matter-Antimatter Studies, Curtin University, Perth, Western Australia 6845, Australia
(Received 7 September 2009; published 7 December 2009)

We apply the convergent close-coupling (CCC) formalism to single-photon two-electron ionization of the lithium atom in its ground state. We treat this reaction as single-electron photon absorption followed by inelastic scattering of the photoelectron on a heliumlike Li^+ ion. The latter scattering process can be described accurately within the CCC formalism. We obtain integrated cross sections of single photoionization leading to the ground and various excited states of the Li^+ ion as well as double photoionization extending continuously from the threshold to the asymptotic limit of infinite photon energy. Comparison with available experimental and theoretical data validates the CCC model.

DOI: 10.1103/PhysRevA.80.063413 PACS number(s): 32.80.Fb, 32.30.Rj, 32.70.−n, 31.15.ve

I. INTRODUCTION

An intimate link of single-photon two-electron ionization and inelastic electron scattering was exploited, to great effect, by various nonperturbative electron scattering theories. Such theories as convergent close coupling (CCC) [1], time-dependent close coupling (TDCC) [2], *R* matrix with pseudostates (RMPSs) [3], and exterior complex scaling [4], developed originally for electron-atom scattering calculations, turned out to be very successful when applied to atomic double photoionization (DPI). Up until recently, these applications were limited to two-electron targets such as the helium [5,6], beryllium, or magnesium [7,8] atoms and the hydrogen molecule [9,10]. In a pioneering development, Colgan *et al.* [11] calculated DPI process in the three-electron lithium atom above the double *K*-shell ionization threshold. Calculated DPI cross section was compared favorably with available experimental data [12–14]. Very recently, a TDCC calculation was reported at several energy points below the double *K*-shell ionization threshold together with RMPS results [15] and in comparison with the experiment [12].

Photoionization applications of the CCC formalism were limited so far to two-electron targets (He and its isoelectronic sequence of ions [16], valence and *K*-shell DPI of alkaline-earth atoms [17,18], and the H_2 molecule [19]). In the CCC formalism, single-photon two-electron ionization is treated as a two step process. The first step is the full absorption of the photon by one electron. The second is inelastic scattering of the photoelectron on the singly charged parent ion which results in promotion of the remaining electron into an excited state or the continuum. DPI calculations on two-electron targets require CCC amplitudes of electron scattering on a singly charged hydrogenic target defined in Ref. [20]. Similarly, DPI calculation on Li requires CCC amplitudes of electron scattering on a He-like Li^+ ion. Generic CCC formalism for electron-He scattering was worked out in Ref. [21]. Specific application to Li^+ ion was made in Ref. [22].

This development paves the way to CCC calculations of two-electron photoionization in Li and similar three-electron targets in which a He-like closed-shell core is augmented by a single valence electron. In the present work, we report our first set of calculations of the total integrated cross sections (TICSs) of various two-electron single and double photoionization processes in the ground-state lithium. Comparison is made with *R*-matrix (RM) calculations of the ground-state photoionization and photoionization with excitation [23] and corresponding experimental data [24]. We then proceed with DPI calculations in the region between the first and second, double *K*-shell, ionization thresholds. We test our DPI cross sections against the experimental results [12,25,26] as well as TDCC and RMPS calculations [15]. In this photon energy range, the DPI process proceeds predominantly via the intermediate singlet or triplet states $1s2s\ ^{1,3}S$ of the Li^+ ion as the overlap of these states with the ground state is the largest. It was argued in [26] that the single photoionization of the triplet state of Li^+ should be the dominant precursor of DPI. This conclusion was based on scaling of the DPI of Li versus DPI of He with the respective ionization potentials of the singly charged ion (^1S or ^3S in the case of Li^+). Our calculated spin-resolved cross sections demonstrate this propensity rule explicitly. Finally, we extend our calculation beyond the second DPI threshold and take it continuously to the asymptotic (nonrelativistic) limit of infinite photon energy. Here we make comparison with theoretical TDCC and RMPS results [15] as well as experiment [12,13].

Even though some theoretical results on single-photon two-electron ionization of Li are available in the literature, we aim at the complete calculation which produces all single and double photoionization cross sections from a consistent set of CCC calculations performed over a wide range of photon energies. The resonant structure due to excitation of the Li^+ hollow states as reported, for instance, in [27] can be, in principle, reproduced by the CCC method. However, this would require an extremely fine photon energy grid and thus make a very laborious task as each photon energy calculation should be carried out separately. An analytic energy dependence of *R*-matrix methods like the one used in [27] makes them much more suitable for such calculations.

*Corresponding author. a.kheifets(at)anu.edu.au

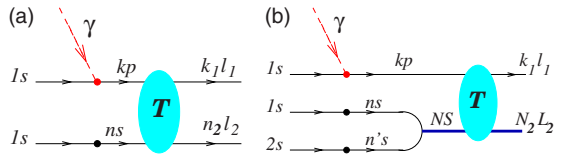

FIG. 1. (Color online) Graphical representation of the amplitudes of single-photon two-electron ionization of He (a) and Li (b).

II. THEORETICAL MODEL

A. General concept

As we have already mentioned in Sec. I, the present application of the CCC method to DPI of Li is a natural extension of our previous work on DPI of He. This connection is illustrated in Fig. 1 where we draw schematically the amplitudes of single-photon two-electron ionizations of He (a) and Li (b). Here we use the following graphical symbols. A thin solid line with an arrow to the right (the direction of time propagation) exhibits a one-electron state. The dashed line indicates a photon. A shaded oval stands for the multiple Coulomb interaction summed to infinite order (the T matrix). Thick solid lines in the Li diagram (b) represent two-electron states.

We first turn to Fig. 1(a) which depicts graphically the DPI process in the helium atom. In the first stage of this process, one of the target $1s^2$ electrons absorbs the whole of the photon and is promoted to a kp continuum state. Another atomic $1s$ electron can overlap with an arbitrary ns bound state of the singly charged He^+ ion. This overlap is indicated by a filled circle. In the second stage of the DPI process, the kp electron scatters inelastically on the ns ionic state. This produces a two-electron state which consists of a continuum Coulomb wave $k_1 l_1$ and a discrete state $n_2 l_2$, which is represented by a hydrogenic pseudostate. Depending on the pseudostate energy, the final two-electron state is attributed either to single photoionization $\epsilon_{n_2 l_2} < 0$ or double photoionization $\epsilon_{n_2 l_2} > 0$.

The CCC treatment of DPI of Li is very similar. The first stage of this process is photoionization of the core $1s$ electron which is far more likely than the ionization of the valence $2s$ electron. This is so because of the proximity to the nucleus which has to absorb the recoil momentum. The two remaining atomic electrons $1s2s$ overlap with various discrete states of the Li^+ ion. These states are represented by the configuration interaction (CI) expansion over pairs of one-electron orbitals,

$$\Psi_\alpha(1,2) = \sum_{nl,n'l'} C^\alpha_{nln'l'} \langle 1||nl\rangle\langle 2||n'l'\rangle, \quad \alpha \equiv NL\mathsf{S}. \quad (1)$$

Here electrons 1 and 2 are assigned to the orbitals nl and $n'l'$, respectively, which are indicated by the Dirac style bra-ket notations $\langle i||nl\rangle \equiv R_{nl}(r_i)$. Spatial exchange as well as angular momentum and spin coupling with the standard Clebsch-Gordan coefficients is absorbed in coefficients $C^\alpha_{nln'l'}$. The two-electron states [Eq. (1)] diagonalize the Li^+ ion Hamiltonian,

$$\langle \Psi_\alpha | H_{Li^+} | \Psi_\beta \rangle = \mathcal{E}_\alpha \delta_{\alpha\beta}. \quad (2)$$

The two-electron states with a given orbital momentum L and spin S are numbered, in increasing energy order, by the integer N. The math serif spin symbol S, which is not displayed in the Li part of Fig. 1, should be distinguished from the angular momentum label S corresponding to $L=0$.

Similarly to DPI of He, the second stage of the DPI of Li proceeds via inelastic electron scattering. However, in the case of He, this is electron scattering on a hydrogenic He^+ ion, whereas in the case of Li this is electron scattering on the He-like Li^+ ion. In both cases, the T matrix includes the Coulomb interaction to infinite order and is found by solving a set of the integral Lippmann-Schwinger equations. The separation of the final channels is performed by examining the two-electron energies: $\mathcal{E}_\alpha < 0$ is attributed to single photoionization, whereas $\mathcal{E}_\alpha > 0$ is the signature of double photoionization.

B. Discrete target states

1. Li atom ground state

In the simplified diagrams of Fig. 1, the ground states of the He and Li atoms are taken to be noncorrelated and are represented by a single configuration of radial Hartree-Fock (HF) orbitals. From our previous work on DPI of He [28], we know that account of the ground-state correlation is important for accurate CCC calculations. This can be achieved by making a multiconfiguration Hartree-Fock (MCHF) expansion of the ground state. In the case of He, this expansion takes the form

$$\Psi_0(1,2) = \sum_{nl} C_{nl} \langle 1||nl\rangle\langle 2||nl\rangle. \quad (3)$$

In Eq. (3), only diagonal terms $(nl)^2$ should be included because the Hartree-Fock ground state is stationary with respect to electron-hole excitations. Only two-electron-two-hole excitations may improve the ground-state energy significantly. A 15-term MCHF expansion recovers 98.9% of the correlation energy in the ground state of He [28]. Deployment of the MCHF ground state [Eq. (3)] in DPI calculations on He is straightforward. The single $1s^2$ configuration in Fig. 1(a) should be substituted by the sum over all possible $(nl)^2$ configurations taken with the corresponding weights C_{nl}. This allows for a wider selection of the intermediate singly ionized states $nlkl'$ coupled to the ground state by the photon absorption.

Similarly, the ground state of Li can be represented by a MCHF expansion

$$\Psi_0(1,2,3) = \sum_{nl\neq 2s} C_{nl} \langle 1||nl\rangle\langle 2||nl\rangle\langle 3||2s\rangle. \quad (4)$$

The wave function [Eq. (4)] includes only pair correlation, i.e., no configurations with all of the three electrons being promoted to vacant states included nor does it contain pair correlation between different atomic shells. A one-hole-one-electron excitation from the K-shell $1s2s3s$ has no significant effect on the ground-state energy. This fact was explained when discussing the MCHF expansion for the ground state of

TABLE I. Ground-state energy and ionization potential of Li from various MCHF expansions.

Configuration	Energy (a.u.)	(%)	IP (eV)
$1s^2 2s$	7.4335	0	4.180
$+1s^1 2s 3s$	7.4335	0	4.181
$+2s 3s^2$	7.4472	30	4.553
$+2s\{3,4\}s^2$	7.4480	32	4.574
$+2s(\{3,4\}s^2+2p^2)$	7.4692	80	5.151
$+2s(\{3,4\}s^2+2p^2+3d^2)$	7.4714	85	5.212
$+2s(\{3,4\}s^2+\{2-4\}p^2+\{3,4\}d^2+4f^2)$	7.4743	92	5.290
Hylleraas[a]	7.4780	100	5.392
Experiment[b]	7.4779	100	5.392

[a]Reference [29].
[b]Reference [30].

He [Eq. (3)]. Only two-electron-two-hole excitations improve the ground-state energy considerably as the number of orbitals in the MCHF expansion [Eq. (4)] grows. This is shown in Table I, where the MCHF ground-state energies (in atomic units) are compared with a more accurate Hylleraas calculation [29] which includes triple correlation. The experimental ground-state energy refers to the sum of ionization potentials of Li I, II, and III taken from the NIST database [30]. The correlation energy (in %) quantifies the gap between the energies of the HF (noncorrelated) state and the exact (or Hylleraas in this particular case) ground state. The ionization potential (in eV) given in Table I is calculated as the difference between the corresponding ground-state energy and the experimental energy of the Li^+ ion. The nine-term MCHF expansion, which includes $n\ell^2$ configurations with $\ell \leq 3$ and $n \leq 4$, recovers 92% of the correlation energy. Further increase of the MCHF basis continues to improve the ground-state energy. However, this has no significant effect on photoionization calculations which will be reported below for the nine-term MCHF expansion.

2. Li^+ ion target states

The two-electron target states [Eq. (1)] are built from one-electron radial orbitals which form the Laguerre basis,

$$\langle r||nl\rangle = \left[\frac{\lambda(n-1)!}{(2l+1+n)!}\right]^{1/2} (\lambda r)^{l+1} e^{-(\lambda r/2)} L_{n-1}^{2l+2}(\lambda r). \quad (5)$$

Here the $L_{n-1}^{2l+2}(\lambda r)$ are the associated Laguerre polynomials and n is restricted by the basis size $n_{\max}$. In the present calculation on the Li^+ ion, the exponential fall-off parameter λ is set to the effective nuclear charge $Z^*=2$ which corresponds to the bare nuclear charge $Z=3$ screened by the remaining target electron.

Wave functions and corresponding energies of the ground and low lying excited states of the Li^+ ion can be calculated up to any desired accuracy by simply increasing $n_{\max}$. In the present section, when testing the target state energies and wave functions against benchmark Hylleraas results, we choose a fairly large $n_{\max}=60$. This, however, is not the entire goal of the present work which is aimed at obtaining convergent photoionization cross sections. These cross sections, reported in the rest of the paper, are obtained with a much more moderate $n_{\max}$ of around 20 at high energies and around 40 at the lowest energies.

TABLE II. Energies (in atomic units) of the lowest NS singlet and triplet two-electron states of the Li^+ ion.

	Singlet states		Triplet states	
N	CCC	Ref. [29]	CCC	Ref. [29]
1	−7.239	−7.279		
2	−5.035	−5.040	−5.109	−5.110
3	−4.732	−4.733	−4.751	−4.752
4	−4.629	−4.629	−4.637	−4.637
5	−4.582	−4.582	−4.586	−4.586
6	−4.556	−4.556	−4.559	−4.559
7	−4.541	−4.541	−4.542	−4.542
8	−4.529	−4.531	−4.530	−4.532
9	−4.513	−4.525	−4.515	−4.525

The spectrum of several lowest discrete two-electron target S states (singlets and triplets) is shown in Table II. Here a comparison is made with the Hylleraas calculation [29]. We observe a generally good agreement between the two sets of calculations. A noticeable difference can be seen for the singlet $1S$ state. This difference shall be attributed to the choice of the exponential fall-off parameter λ in Eq. (5) corresponding to the effective nucleus charge $Z^*=2$. This choice of Z^* is natural when the "outer" target electron sees the bare nucleus charge screened by the "inner" electron. However, the dominant configuration of the $1S$ state is $1s^2$ when both electrons occupy the same orbital and cannot be treated as inner or outer.

In addition, some variation between the presently calculated ionic energies and that reported in Ref. [29] can be detected at fairly large N. This happens because the Hylleraas spectrum is related to the true target states. This spectrum converges to the ionization limit of Li^+ at 4.5 a.u. as is shown in the top panels of Fig. 2. On the other hand, the CCC energies are related to pseudostates diagonalizing the target Hamiltonian (2). This spectrum does not have a condensation point and is continued above the ionization threshold by positive-energy pseudostates (see the same plots).

Another test of the Li^+ target states can be performed against the asymptotic ratios of partial photoionization cross sections σ_α relative to the total cross section σ taken in the infinite photon energy limit. These ratios can be calculated as [29]

$$R_\alpha = \left.\frac{\sigma_\alpha}{\sigma}\right|_{\omega\to\infty} = \frac{c_\alpha}{c}, \quad (6)$$

where

$$c_\alpha = |\langle \Psi_0(1,2,3)|\delta(\boldsymbol{r}_3)|\Psi_\alpha(1,2)\,|^2,$$

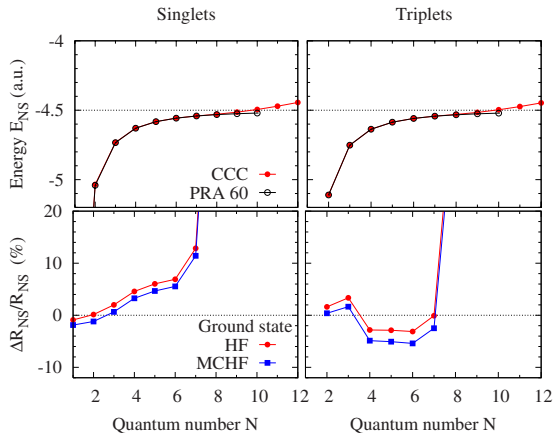

FIG. 2. (Color online) Two-electron target state energies E_{NS} (top) and relative error of the asymptotic coefficients $\Delta R_{NS}/R_{NS}$ with respect to the Hylleraas values [29] (bottom) for the singlet (left) and triplet (right) states. For the bottom plots, the ground state is taken either in the HF or MCHF approximation.

$$c = \langle \Psi_0(1,2,3) | \delta(\boldsymbol{r}_3) | \Psi_0(1,2,3) \rangle. \tag{7}$$

Here $\alpha \equiv NS$ since non-S target states have vanishing partial cross sections in this high photon energy limit. In this limit, to facilitate exchange of a large recoil momentum with the nucleus, the photoelectron is removed predominantly from the close vicinity to the origin where higher L states are suppressed by the centrifugal barrier.

The sum over all the positive and negative energy ion states can be carried over using the completeness of this basis (the closure relation) resulting in $\Sigma_\alpha c_\alpha = c$. The negative energy part of the pseudostate spectrum is related to the singly charge Li^+ ion states, whereas the positive-energy part of the spectrum can be attributed to multiply ionized states. Since the triple photoionization is much less likely than DPI, we can equate the whole of multiple photoionization with the yield of the DPI channel. Then, the double-to-single asymptotic cross-section ratio can be expressed as [29]

$$R_{21} = \frac{\sigma^{2+}}{\sigma^{+}} = \frac{c - \sum_\alpha c_\alpha}{\sum_\alpha c_\alpha}. \tag{8}$$

Here only negative energy states $\mathcal{E}_\alpha$ are included in the sum. Because the ratios [Eqs. (6) and (8)] are expressed via the atomic ground-state wave function, their accuracy can be used as a test on the MCHF approximation. The ratios R_α for various singlet and triplet states and the double-to-single ratio R_{21} are given in Table III in comparison with analogous values from a more accurate Hylleraas calculation [29]. Because of divergence of the pseudostate and eigenstate energies near the ionization threshold as is seen in the top panels of Fig. 2, the error of the asymptotic ratios relative to the Hylleraas values is increasing (see bottom panels of Fig. 2). That is why only a limited number of NS states (up to $N=9$ in our case) could be included reliably when calculating the ratio R_{21} according to Eq. (8). To test the accuracy of this limited summation, we also computed this ratio with the Hylleraas data [29] and compared this calculation with a much more extended summation reported in the same work. Fortunately, because of a very rapid fall of R_{NS} with N, thus calculated double-to-single ratio $R_{21}^9 = 0.0325$ is very close to the one evaluated from the infinite sum $R_{21}^\infty = 0.0336$. We expect it to be the case in our calculation as well. When comparing the HF and MCHF results for R_α and R_{21}, we see some improvement of the five-term MCHF expansion over noncorrelated HF ground state. It is particularly noticeable in the case of the double-to-single ratio.

C. Photoionization amplitudes

To take advantage of the explicit spin dependence of the two-electron target states [Eq. (1)], we ought to match it with

TABLE III. Asymptotic partial photoionization ratios R_α for various $\alpha \equiv NS$ and the double-to-single ratio R_{21} in the limit of infinite photon energy. The single digit in place of the decimal point indicates the number of zeros to be inserted after the point.

	Singlet states			Triplet states		
N	HF	MCHF	Ref. [29]	HF	MCHF	Ref. [29]
1	$0_1$1217	$0_1$1205	$0_1$1228			
2	0.2092	0.2064	0.2089	0.5498	0.5432	0.5411
3	$0_1$3166	$0_1$3124	$0_1$3104	0.1700	0.1672	0.1645
4	$0_3$9993	$0_3$9867	$0_3$9556	$0_2$4426	$0_2$4333	$0_2$4555
5	$0_3$2865	$0_3$2828	$0_3$2702	$0_2$1416	$0_2$1384	$0_2$1458
6	$0_3$1252	$0_3$1236	$0_3$1171	$0_2$6488	$0_3$6335	$0_3$6697
7	$0_4$7061	$0_4$6970	$0_4$6256	$0_2$3690	$0_3$3601	$0_3$3693
8	$0_4$6565	$0_4$6481	$0_4$3775	$0_2$3334	$0_3$3252	$0_3$2275
9	$0_4$7419	$0_4$7323	$0_4$2472	$0_3$3931	$0_3$3833	$0_3$1509
Σ_1^9	0.2546	0.2513	0.2536	0.7274	0.7178	0.7130
R_{21}^9	0.0179	0.0309	0.0325			
R_{21}^∞			0.0336			

a similar dependence in the three-electron ground state. To this end, we write the ground-state wave function [Eq. (4)] in the fully symmetrized form,

$$\begin{aligned}\sqrt{3}\Psi_0(1,2,3) &= \langle 1,2|1s^2\ ^1S\rangle\langle 3||2s\rangle - \langle 1,3|1s^2\ ^1S\rangle\langle 2||2s\rangle \\ &+ \langle 2,3|1s^2\ ^1S\rangle\langle 1||2s\rangle \\ &= \frac{1}{\sqrt{2}}[\langle 1,2|1s2s\ ^3S_{M_S=0}\rangle - \langle 1,2|1s2s\ ^1S\rangle]\langle 3||1s\rangle \\ &- \langle 1,2|1s2s\ ^3S_{M_S=1}\rangle\langle 3||1s\rangle \\ &+ \langle 1,2|1s^2\ ^1S\rangle\langle 3||2s\rangle. \end{aligned} \quad (9)$$

Here we coupled electrons 1 and 2 into a definite spin state. For brevity of notations, we consider here a noncorrelated HF ground state. Incorporation of the ground-state correlations implemented by the MCHF expansion [Eq. (4)] is straightforward. The main $1s^2$ configuration should be augmented by all nl^2 configurations taken with corresponding weights.

The final state wave function is written in a nonsymmetrized form as

$$\Psi_f(1,2,3) = \langle 1,2|\alpha\rangle\langle 3||kl\rangle,$$

where k, l are the linear and angular momenta of the photoelectron. By factoring out angular momentum and spin projection dependence using standard summation techniques [31], we can define the dipole matrix elements for singlet and triplet channels,

$$\begin{aligned} d_{\alpha l}(k) &= (-1)^{S+1}\sqrt{\frac{2S+1}{2}}\langle 1s2s\ ^{2S+1}S1s|\left|\sum_{j=1}^{3} r_j\right||\alpha kl\rangle \\ &+ \langle 1s^2\ ^1S2s|\left|\sum_{j=1}^{3} r_j\right||\alpha kl\rangle\delta_{S0}. \end{aligned} \quad (10)$$

The three-electron dipole matrix elements [Eq. (10)] can be factored out into the products of two-electron and one-electron matrix elements,

$$\begin{aligned}\langle 1s2s\ ^{1,3}S2s|\left|\sum_j r_j\right||\alpha kl\rangle &= \langle 1s2s\ ^{1,3}S||r_1+r_2||\alpha\rangle\langle 2s||kl\rangle \\ &+ \langle 1s2s\ ^{1,3}S||\alpha\rangle\langle 2s||r||kl\rangle, \end{aligned}$$

$$\begin{aligned}\langle 1s^2\ ^1S2s|\left|\sum_j r_j\right||\alpha kl\rangle &= \langle 1s^2\ ^1S||r_1+r_2||\alpha\rangle\langle 2s||kl\rangle \\ &+ \langle 1s^2\ ^1S||\alpha\rangle\langle 2s||r||kl\rangle. \end{aligned}$$

The two-electron matrix elements can be further simplified using the CI expansion [Eq. (1)]. For instance, the two-electron overlaps can be written as

$$\langle 1s^2\ ^1S||\alpha\rangle = \sum_{nl,n'l'} C^{\alpha}_{nln'l'}\langle 1s||nl\rangle\langle 1s||n'l'\rangle\delta_{l0}\delta_{l'0}\delta_{S0},$$

$$\begin{aligned}\langle 1s2s\ ^{1,3}S||\alpha\rangle &= \frac{1}{\sqrt{2}}[\langle 1s||1\rangle\langle 2s||2\rangle + (-1)^S\langle 1s||2\rangle\langle 2s||1\rangle] \\ &\times \sum_{nl,n'l'} C^{\alpha}_{nln'l'}\langle nl||1\rangle\langle nl||2\rangle \\ &= \sqrt{2}\sum_{nn',ll'} C^{\alpha}_{nln'l'}\langle 1s||nl\rangle\langle 2s||n'l'\rangle\delta_{l0}\delta_{l'0}. \end{aligned}$$

Here we used the exchange properties of the CI coefficients $C^{\alpha}_{nln'l'} = (-1)^S C^{\alpha}_{n'l'nl}$. Same rules apply to the two-electron dipole matrix elements.

Similar techniques can be employed to calculate the coefficients c_α entering expressions for the asymptotic ratios [Eqs. (6) and (8)]. In this case, the one-electron dipole operator r entering expression (10) should be substituted with the radial delta-function operator $\delta(r)$. We then arrive at the following expressions:

$$\begin{aligned} C_\alpha &= \frac{2S+1}{2}|(-1)^{S+1}\langle 1s2s\ ^{2S+1}S||\alpha\rangle\langle 0||1s\rangle \\ &+ \sqrt{2}\langle 1s^2\ ^1S||\alpha\rangle\langle 0||2s\rangle\delta_{S0}|^2. \end{aligned} \quad (11)$$

In the above the ground-state radial orbitals $1s$ and $2s$ are taken at the origin $\langle 0||ns\rangle \equiv \langle r=0||ns\rangle$.

We write the dipole matrix element in Eq. (10) in the length (L) gauge. Alternatively, the dipole operator can be chosen in the velocity (V) gauge $\omega^{-1}\Sigma_{j=1}^{3}\nabla_j$. Convergence between the calculations in the two gauges serves as a useful test of the accuracy of the ground and final state wave functions.

Final state correlations which are indicated by the shaded oval in Fig. 1 are accounted for by integration of the "bare" dipole matrix elements [Eq. (10)] with the T matrix,

$$D_{\alpha l}(k) = d_{\alpha l}(k) + \sum_{\beta l'}\int_{k'}\frac{\langle \alpha lk||T||\beta l'k'\rangle d_{\beta l'}(k')}{E - k'^2/2 - \mathcal{E}_\beta + i\delta}. \quad (12)$$

Here $E = k^2/2 + \mathcal{E}_\alpha$ is the total energy of the scattering system which consists of the photoelectron and the Li^+ ion. Only dipole channels are included in Eq. (12) which correspond to the total angular momentum of the scattering system $\mathcal{L}=1$ and the spin $\mathcal{S}=1/2$. The T matrix is found by solving a set of the integral Lippmann-Schwinger equations [32]. The partial photoionization cross section to a given final channel is written as

$$\sigma_\alpha(\omega) = \frac{4\pi^2\omega}{3c}\sum_l \int d^3k|D_{\alpha l}(k)|^2\delta(\omega - E_\alpha - k^2/2 + E_0), \quad (13)$$

where $c \simeq 137$ is the speed of light in atomic units.

III. RESULTS

A. Below double *K*-shell transition onset

We first concentrate on the region above the first double ionization threshold at 81.0 eV [30] but below the onset of Rydberg states converging to the double K-shell ionization

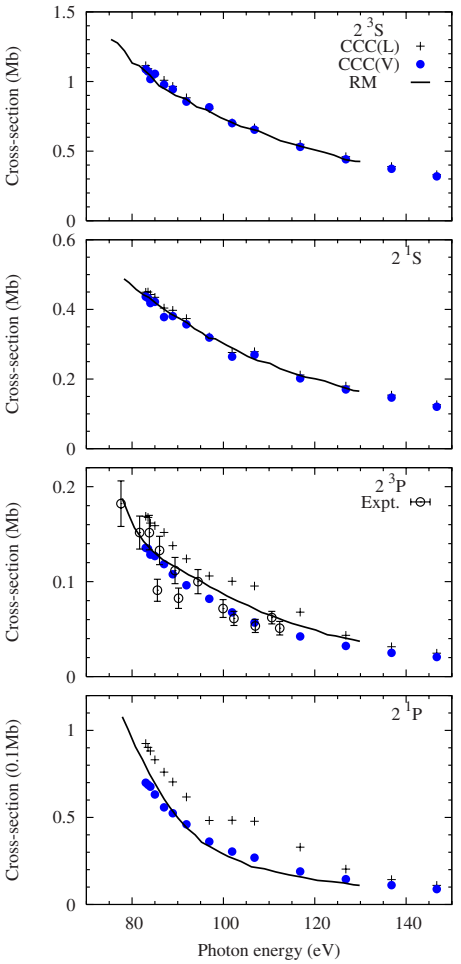

FIG. 3. (Color online) Partial photoionization cross sections corresponding to the Li^+ ion left in the $2\ ^3S$, $2\ ^1S$, $2\ ^3P$, and $2\ ^1P$ states (from top to bottom). The plotting symbols are as follows: crosses—CCC(V), filled circles—CCC(L), solid line—RM calculation [23], and open circles with error bars—experiment [24].

threshold which starts at about 150 eV [27]. At this photon energy range, the most dominant two-electron photoionization processes involve transitions of the $1s$ and $2s$ electrons leaving the remaining $1s$ in the same quantum state. In practical calculations, however, we relaxed the core to include also the $2s$ orbital. We have done so to cover the whole photon energy range with one set of consistent CCC calculations. This range includes the photon energies above the second DPI threshold at 172.8 eV where the double K-shell ionization becomes the dominant channel.

The CCC calculations reported in this paper correspond to the Laguerre basis [Eq. (5)] with $l_{max}=3$ and n_{max} being around 40 at the lowest considered energies and decreasing systematically to around 20 at the highest energies.

1. Single photoionization

The partial photoionization cross sections leaving the Li^+ ion in the four lowest excited states $2\ ^{1,3}S$ and $2\ ^{1,3}P$ are shown in Fig. 3. Comparison is made with RM calculations [23] and, where available, with experimental data [24]. In this figure, we adopt the conventional spectroscopic notations $N\ ^{2S+1}L$. In the following figures, we also label the Li^+ ion states by the dominant pair of one-electron orbitals entering expansion [Eq. (1)], i.e., the $2S$ state corresponds to the dominant $1s2s$ configuration. As we observe from Fig. 3, the CCC results in the V gauge are generally in good agreement with the available literature data. The L-V gauge convergence worsens as the final ionic state becomes excited further away from its ground state (from the top to bottom panels of Fig. 3). This is so because the ionization-excitation process is more affected by many-electron correlations than the ground-state ionization. In the former process, both atomic electrons change their quantum states whereas the latter process involves only a one-electron transition. The gauge divergence becomes even a more serious issue for the DPI process which is entirely driven by correlations. This issue will be discussed in Sec. III A 2.

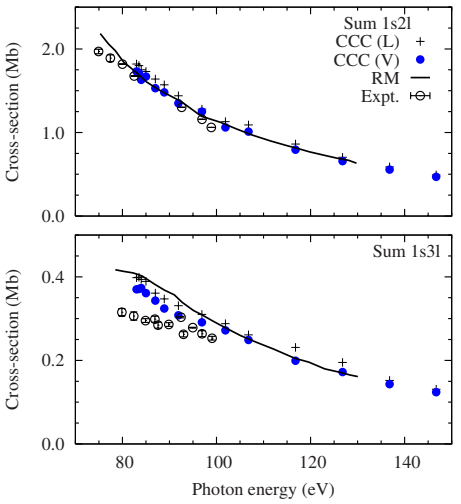

FIG. 4. (Color online) Partially summed photoionization cross sections leading to various $1s2\ell$ (top) or $1s3\ell$ (bottom) Li^+ ion states. The plotting symbols are the same as in Fig. 3.

Partially summed single photoionization cross sections leading to various $1s2\ell$ or $1s3\ell$ ionic states are shown in Fig. 4 (top and bottom panels, respectively) in comparison with the R-matrix theory [23] and the experiment [24]. Here again a good agreement between the CCC and R-matrix calculations can be seen. Experimental data are close to both calculations for the $1s2\ell$ cross section sum but lie noticeably below the two theories for the $1s3\ell$ sum.

Apart from total ionization cross sections, the single photoionization process can be characterized by the angular asymmetry β parameter which defines the photoelectron angular distribution. In the case of linearly polarized photons, this distribution takes the form [33]

$$\frac{d\sigma}{d\Omega} = \frac{\sigma}{4\pi}[1 + \beta P_2(\cos\theta)]. \tag{14}$$

Corresponding β parameters, as functions of photon energy, are plotted in Fig. 5 for the lowest $2\ ^{1,3}P$ ionic states in comparison with the RM theory [23] and the experiment [24]. Here the RM and CCC(V) theories lend support to each other but the experimental β parameters are somewhat be-

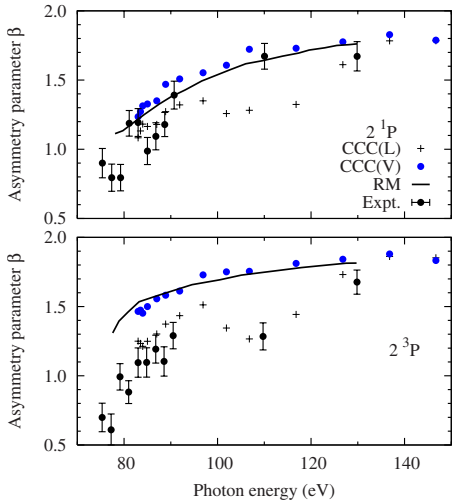

FIG. 5. (Color online) Angular asymmetry β parameters for the single photoionization to the $2\,^1P$ (top) and $2\,^3P$ (bottom) ionic states. The plotting symbols and the literature data sources are the same as in Figs. 3 and 4.

low. We have no plausible explanation of the origin of this disagreement with the experiment also seen in the bottom panel of Fig. 4.

2. Double photoionization

In Fig. 6 we present the CCC results for the single, double-to-single ratio, and double photoionization cross sections (from top to bottom). Comparison is made with experimental data [12,26] and recent RMPS and TDCC calculations [15].

We see that the L-gauge results, especially strong for DPI, deviate from the V gauge. As was observed in our earlier work on DPI of He [28], even very extensive MCHF expansions were not sufficient to produce convergent L-gauge results even though the CCC basis was fully converged. A much more accurate Hylleraas-type ground-state wave function is needed for this purpose. Although such a wave function can be constructed [29], we were unable to incorporate it in our present calculation.

The role of the ground-state correlation is different in the two main DPI mechanisms: the knockout (KO) and shake off (SO) [34]. The KO mechanism, exhibited graphically by the diagrams of Fig. 1, is not particularly sensitive to the ground-state correlation. Conversely, the SO mechanism, in which the two electrons are ejected into the continuum without any interelectron interaction, is strongly dependent on this type of correlation. The slow KO mechanism is prevalent near the DPI threshold, whereas the fast SO mechanism is dominant at large photon energies. That is why we expect the two gauges to be close for near-threshold CCC calculations whereas the L gauge can become unreliable away from the threshold.

The SO and KO processes are represented by the first and second terms in the right hand side of Eq. (12), respectively. The first bare term does not involve any interelectron interaction and propagates both electrons into continuum solely via the SO process. The second integral term does contain

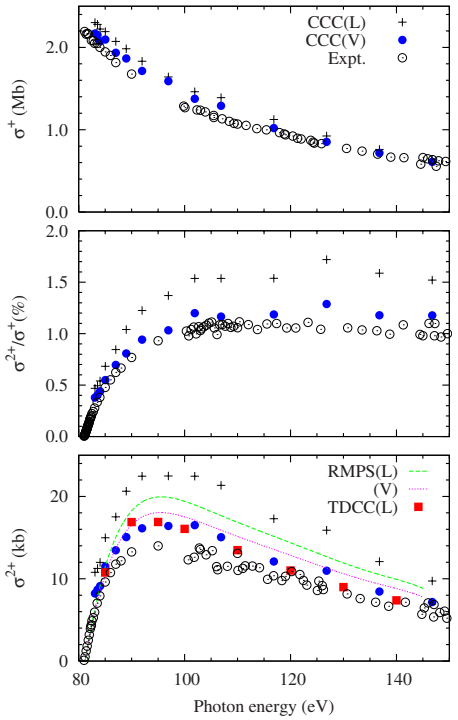

FIG. 6. (Color online) Single photoionization cross section of Li (top panel), double-to-single photoionization cross-section ratio (middle panel), and double photoionization cross section (bottom panel). Comparison of the CCC calculation is made with experiment [12,26] as well as RMPS and TDCC calculations [15] (bottom panel only). The plotting symbols are as follows: crosses—CCC(L), filled circles—CCC(V), dashed line—RMPS(L), dotted line—RMPS(V), filled squares—TDCC(L), and open circles—experiment.

the interelectron interaction to infinite order and thus is responsible for the electron impact ionization of the singly charge Li^+ ion which constitutes the KO process. The photoionization cross section [Eq. (13)] contains the squared matrix element [Eq. (12)] and, thus, the interference term of the SO and KO amplitudes. This interference, generally, precludes an unambiguous separation of the KO and SO ionization processes. However, in the near-threshold and high-energy regions, this separation is quite clear (see, e.g., Ref. [35]).

Our V-gauge calculation for σ^{2+}, shown in the bottom panel of Fig. 6, agrees very well with the TDCC calculation for which only the L gauge is shown as both gauges are within 1% error margin. The RMPS(V) calculation is also quite close except for the largest photon energies presented in the figure. The RMPS(L) calculation is further apart but not as much as the CCC(L) calculation. This is so because the quality of the ground state employed in the RMPS model is better compared to the CCC model as could be seen from the corresponding ionization potentials (CCC: 5.212 eV, RMPS: 5.410 eV, and experiment: 5.392 eV).

The experimental DPI cross section [12,26] is noticeably below both the CCC(V) and TDCC(V) results. Colgan *et al.* [15] discussed this difference and attributed it to calibration of the single photoionization cross section σ^+ which was used to convert the experimental double-to-single ratio to the

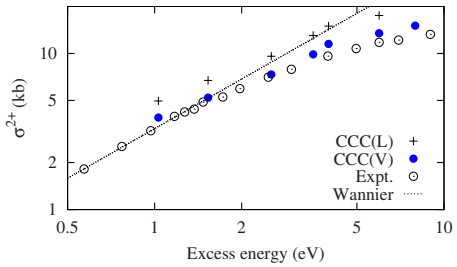

FIG. 7. (Color online) Double photoionization cross section as a function of the excess energy in the near-threshold region. The plotting symbols are as follows: crosses—CCC(L), filled circles—CCC(V), and open circles—experiment [26]. The Wannier threshold law [Eq. (15)] is drawn with a dotted line.

absolute σ^{2+} cross section. We see indeed that the experimental ratio σ^{2+}/σ^{+}, shown in the middle panel of Fig. 6, is closer to the CCC(V) calculation as compared to the corresponding data for the absolute σ^{2+} cross section. Wehlitz *et al.* [26] used for calibration the value of $\sigma^{+}=1.22 \pm 0.12$ Mb at $\omega=103.3$ eV [36] which should be compared with a somewhat larger CCC(V) value of 1.34 Mb. This difference of single photoionization cross sections magnifies a moderate, of the order of 10%, difference between the CCC(V) and experimental double-to-single photoionization cross-section ratios.

3. Wannier threshold law

DPI of Li in the near-threshold region received special attention. Wehlitz *et al.* [25] examined carefully the DPI cross section within the interval of 2 eV above the threshold. They tested the Wannier threshold law,

$$\sigma^{2+}(E) = \sigma_0 E^{\gamma}, \tag{15}$$

which should govern the DPI cross-section dependence on the excess energy above the threshold. They fit their data with Eq. (15) using the exponent $\gamma=1.056$ which should correspond to the effective nucleus charge $Z^{*}=2$. The preexponential factor was found to be $\sigma_0=3.3$ kb. In addition, Wehlitz *et al.* [25] reported systematic oscillation of their data around the Wannier threshold law. This modulated threshold law was originally explained by unequal binding energies of the electrons involved in the DPI process on Li. Later, this explanation was retracted [37].

We show our near-threshold calculations in Fig. 7 where we plot the DPI cross section versus the excess energy above the DPI threshold. We also plot the experimental data and the Wannier threshold law [Eq. (15)] with γ and σ_0 parameters reported in Ref. [25]. We see our data approaching the Wannier exponent which, in double logarithmic scale, makes a straight line. However, in the present calculation, we were not able to reach the excess energies below 1 eV. This would require presence of both the very small (for continuum discretization) and very large (convergence in Li^{+} ground-state) positive-energy pseudostates in the CCC basis which was not possible to achieve at the same time.

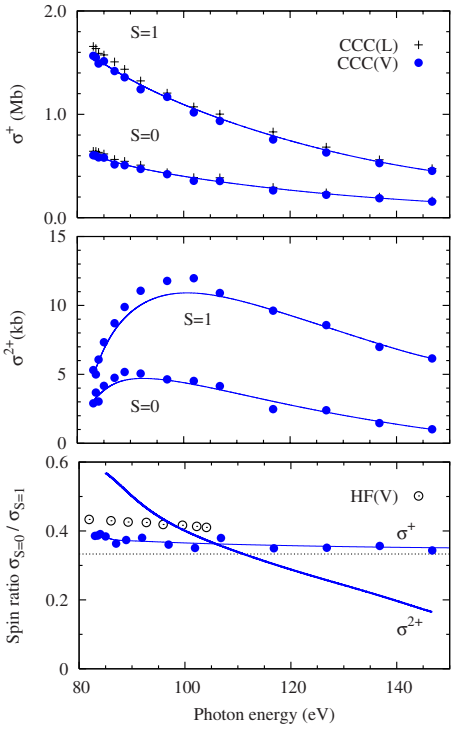

FIG. 8. (Color online) Spin resolved single and double photoionization cross sections (top and middle panels) and singlet-to-triplet spin ratios (bottom panel). Raw CCC results in the top and middle panels are shown with crosses (length) and filled circles (velocity). The solid lines in three panels represent the Bezier smoothed V-gauge results. The Hartree-Fock V-gauge results for single photoionization spin ratio [24] are displayed with open circles in the bottom panel. The dotted line represents the statistical ratio 1/3.

4. Spin asymmetries

Explicit spin dependence of the Li^{+} target states in the CCC model allows readily for separation of the singlet and triplet photoionization channels. Spin resolved singlet and triplet photoionization cross sections are shown in Fig. 8. In the top panel, we show the single photoionization cross section in the L and V gauges separated into singlet and triplet channels. In the middle panel, we show the spin-resolved DPI cross sections in the V gauge since the L gauge looses its accuracy for DPI calculations in this photon energy range.

The singlet-to-triplet spin ratio for single photoionization is rather flat as a function of the photon energy. This ratio value, in the V gauge, is about 0.35 which is fairly close to the statistically determined ratio of 1/3. The latter is simply the spin projection ratio between the singlet and triplet states embedded into Eq. (10). In the limit of infinite photon energy, the singlet-to-triplet ratio takes the asymptotic value of 0.36 as can be calculated from entries Σ_1^9 in Table III. This fairly steady ratio which is hardly changing across the whole photon energy range can be interpreted in the following way. The dipole matrix elements [Eq. (10)] and the asymptotic coefficients [Eq. (11)] are calculated from similar formulas which only differ by the radial operator [r and $\delta(r)$, respectively]. The terms containing these operators are the same for

the singlet and triplet channels. What differentiate these channels are the overlaps between the ground atomic state and singly ionized target states entering expressions for the dipole matrix elements [Eq. (10)] and the asymptotic coefficients [Eq. (11)]. In the latter case we can use the following numerical values $\langle 0||1s\rangle = 9.23$, $\langle 0||2s\rangle = 1.45$ which allow us to attribute the main difference between the singlet and triplet channels to the overlaps $\langle 1s2s\ ^{2S+1}S|\alpha\rangle$. For the most dominant singly ionized $2S$ channel, these overlaps are 0.92 and 0.86 for the singlet and triplet states, respectively. This explains a slight increase of the singlet-to-triplet ratio from the statistical value 1/3 up to 0.35 by the overlap factor.

The spin ratio for DPI shows more substantial photon energy dependence which decreases continuously from the near-threshold value of close to one and falling below the kinematic ratio of 1/3 at larger photon energies. Given the steady singlet-to-triplet ratio in the single ionization channels, varying ratio in the DPI channel can be attributed to spin flip scattering processes accompanying electron impact ionization of Li^+. Note that the two-electron spin S is not a conserved quantity, whereas the total spin of the scattering system $\mathcal{S}=1/2$ is. Unfortunately, the closure relation cannot be used separately for singlet and triplet channels. Therefore, the spin asymmetry ratio in the DPI channel cannot be extracted from entries of Table III and thus tested in the infinite photon energy limit.

5. Scaling with helium

Wehlitz *et al.* [26] demonstrated that their near-threshold double-to-single photoionization cross-section ratio in Li can be scaled with analogous ratio in He when plotted versus the reduced excess energy $\Delta E = E/\mathcal{V}_{Li^+\ 1s2s}$, where $\mathcal{V}$ represents the ionization potential. Here the ionization potential of Li^+ $1s2s$ ion is calculated as the difference of the double and single ionization potentials of the neutral lithium atom. Since the Li^+ $1s2s$ ion can be found in two different spin states, singlet and triplet, the corresponding ionization potentials of $\mathcal{V}_{Li}=66.31$ and 64.41 eV can be alternatively used to calculate the unit measuring the reduced excess energy ΔE. Only one such ionization potential exists in the case of helium.

Wehlitz *et al.* [26] observed that using the single ionization potential of Li corresponding to the triplet $1s2s\ ^3S$ ion state produced a more accurate scaling with the helium data [38]. In Fig. 9 we scale our double-to-single photoionization cross-section ratio, in the velocity gauge, with the Li and He experimental data. Both our CCC(V) results and the Li experimental data [26] can be scaled very accurately to the He data [38] albeit with slightly different scaling factors (0.32 and 0.28, respectively).

A slight numerical noise of our data does not allow us to discriminate between the two possible ionization potentials based on the quality of scaling with He as was done in Ref. [26]. However, our spin-resolved cross sections shown in Fig. 8 indicate explicitly that the triplet singly ionized state is indeed the dominant precursor of DPI of Li.

B. Above the second DPI thresholds

At photon energy above the second DPI threshold at 172.8 eV, the double K-shell photoionization becomes the dominant channel. Our results in this photon energy range are shown in Fig. 10 together with theoretical and experimental data available in the literature. In the top panel of Fig. 10 we plot the single photoionization cross section in comparison with experimental data [12]. Our calculations in both gauges agree between each other but the calculated cross sections exceed the measured one by about 20% below the 300 eV photon energy mark. The double-to-single cross-section ratio in the V-gauge remains largely flat and its value is generally consistent with the experiment [13]. The L gauge deviates from the V gauge similarly to the lower photon energy calculation displayed in Fig. 6. The DPI cross section in

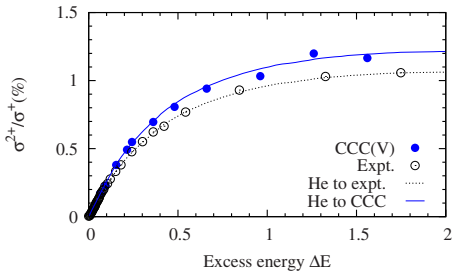

FIG. 9. (Color online) Double-to-single photoionization cross-section ratios plotted versus the reduced excess energy ΔE. The CCC data, in the V gauge, are plotted with filled circles. The Li experimental data [26] are shown with open circles. The He experimental data [38] are scaled to the Li experiment and the CCC(V) calculation and drawn with dotted and solid lines, respectively.

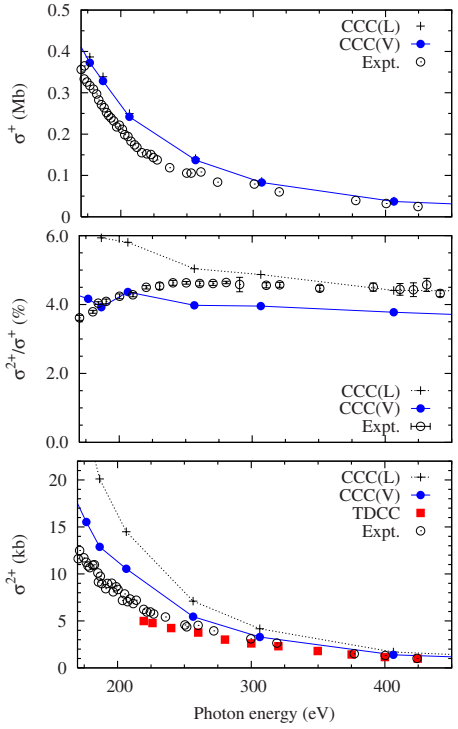

FIG. 10. (Color online) Single photoionization cross-section of Li (top panel), double-to-single photoionization cross-section ratio (middle panel), and DPI cross section (bottom panel). The plotting symbols are as follows: crosses—CCC(L), filled circles—CCC(V), filled squares—TDCC calculation [39], and open circles—experiment [12,13].

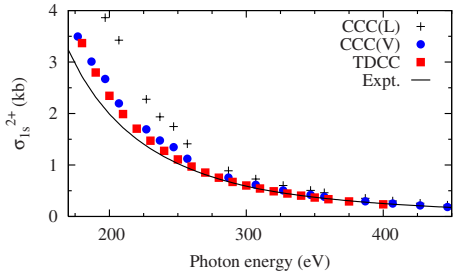

FIG. 11. (Color online) DPI cross section corresponding to the Li^{2+} ion left in the ground $1s$ state. The plotting symbols are the same as in Fig. 10 except for the black solid line which corresponds to a phenomenological model of Ref. [14].

the V gauge exceeds the experimental data by approximately the same amount as in the single photoionization channel. That is why the ratio of the double-to-single cross sections is more consistent between the theory and experiment. Above the 300 eV energy mark, CCC calculations in both gauges tend to converge and agree well both with experimental data of [12,13] and the TDCC calculation [39].

In the photon energy range above the second DPI threshold, the residual Li^{2+} ion can be left in various final states. In their theoretical paper, Colgan *et al.* [39] reported partial DPI cross sections corresponding to the ground $1s$ and excited $2s$, $2p$ ionic states. Using the scaling to He, Wehlitz *et al.* [14] separated the ground-state contribution from their experimental DPI cross section and found a generally good agreement with the TDCC calculation [39]. In Fig. 11 we show CCC(L) and CCC(V) results for the partial DPI cross section leading to the Li^{2+} $1s$ state. This calculation is performed with the frozen core CI basis [Eq. (1)] in which one of the target electrons is restricted to the $1s$ state. The CCC(V) results are generally consistent with the experiment and very close to the TDCC calculation [39]. Above the 300 eV mark, both gauges of the CCC model tend to converge.

Infinite photon energy limit

Photoionization cross-section calculations in the region of very large photon energies can be tested using the asymptotic ratios R_α with $\alpha \equiv NS$ for ionization excitation [Eq. (6)] and R_{21} for DPI [Eq. (8)]. In Fig. 12, we display the partial ionization-excitation cross-section ratios to various singlet (top panel) and triplet (middle panel) NS channels normalized to the total photoionization cross section. The CCC calculation covers continuously the photon energy range from the second DPI threshold to 2 keV. The asymptotic ratios of Table III corresponding to the infinite photon energy limit are displayed in the same panels by arrows. To accommodate the infinite photon energy limit, we distort the photon energy scale by making the equal intervals of the inverse photon energy equidistant. This explains the condensation of the photon energy marks toward the right end of the scale. We see little variation of partial photoionization-excitation ratios in the logarithmic scale which we have to adopt for the two top panels of Fig. 12 to display several orders of magnitude decline of the ratio R_{NS} with N. The double-to-single ratio σ^{2+}/σ^{+}, when plotted in the linear scale in the bottom panel,

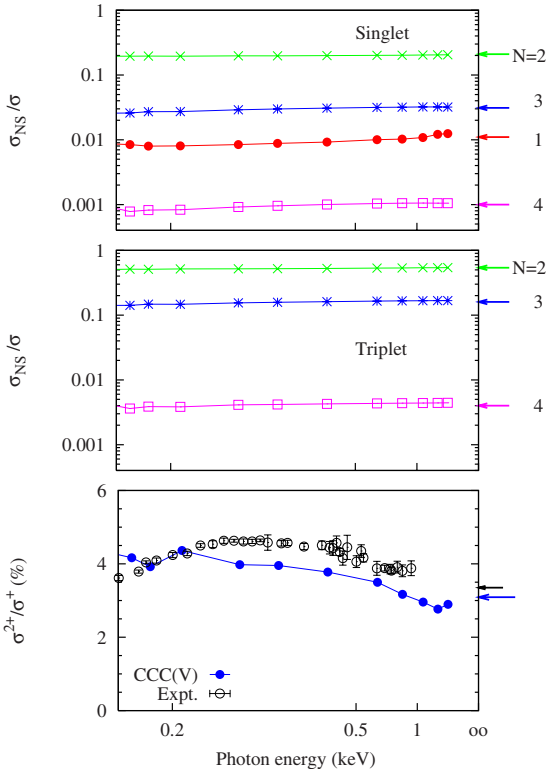

FIG. 12. (Color online) Partial photoionization cross-section ratios (V-gauge singlet channels—top panel; triplet channels—middle panel) and double-to-single ratio (also V-gauge, bottom panel) plotted versus the photon energy. The horizontal scale is compressed toward large photon energies by making the equal intervals of the inverse photon energy equidistant. The experimental data in the bottom panel are from Ref. [13]. Corresponding infinite photon energy limits R_{NS} in the top and middle panels and R_{21} in the bottom panel are indicated with arrows.

varies noticeably. The experimental ratio seems to be compatible with the theoretical asymptotic limit of $R_{21}=3.3\%$ [29] (short arrow), whereas the CCC(V) calculation seems to be somewhat below our own calculated result $R_{21}=3.1\%$ (long arrow).

Finally, in Fig. 13 we plot our DPI results across the whole excess energy range studied in the present work starting from 1 eV above the first DPI threshold and taking it continuously to 2 keV excess energy. We see that the CCC(V) calculation is able to reproduce the experimental data [12–14] reasonably well. The only noticeable disagreement is a somewhat smaller double-to-single ratio above the second DPI threshold. This can be attributed to the frozen core approximation adopted in the present work which restricts the remaining target electron in the Li^{2+} ion to the $1s$ or $2s$ states.

IV. CONCLUSION AND FURTHER DIRECTIONS

In the present work, we developed and tested a CCC model of single-photon two-electron ionization of the lithium atom in its ground state. The model assumes that the photon is absorbed by one of the target electrons which is then pro-

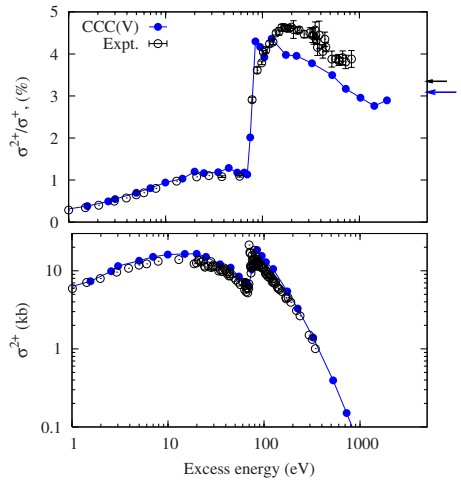

FIG. 13. (Color online) Double-to-single photoionization cross-section ratio (top panel) and the DPI cross section (bottom panel) plotted versus the excess energy above the first DPI threshold. The CCC calculation in the *V* gauge is compared with experimental data [12–14]. The experimental and theoretical infinite photon energy limits of the ratio are indicated in the top panel with the short and long arrows, respectively.

moted to an excited state or the continuum. At the second stage of the reaction, the photoelectron scatters inelastically on the singly charged Li^+ ion. The latter scattering process can be described adequately by the CCC model.

We performed a consistent set of CCC calculations for various photon energies ranging from the threshold and reaching continuously the asymptotic infinite energy limit. We employed the dipole operator in the length and velocity gauges. We explored the partial ionization-excitation cross sections, angular and spin asymmetries, and double photoionization cross sections in various photon energy regimes. Wherever possible, we used literature data to subject our model to a stringent test. In general, good agreement with available theoretical and experimental results is found which demonstrates validity of the present model.

Some further developments can be done to improve the accuracy of the CCC DPI results. A more extended frozen core basis is needed to achieve the full convergence of the CCC results above the second DPI threshold. At the moment, we are not able to perform such extended calculations due to computational constraints. Also, a more accurate Hylleraas-type ground state is desirable to improve the *L*-gauge results. Apart from these technical developments, we would like to perform energy and angular resolved calculations to obtain fully differential DPI cross sections which are now can be measured experimentally [40]. We also want to explore other targets beyond lithium in which a heliumlike core is augmented by a single valence electron. Such elements (B, Al, etc.) can be found in the third group of the Periodic Table. We would also like to perform ionization-excitation, autoionization, and double ionization calculations on three-electron targets by fast projectile impact. This will be a natural extension of our previous work on two-electron targets [41–43].

ACKNOWLEDGMENTS

We thank Ralf Wehlitz and James Colgan for communicating their data in numerical form. Resources of the National Computational Infrastructure (NCI) Facility were used.

[1] I. Bray, D. V. Fursa, A. S. Kheifets, and A. T. Stelbovics, J. Phys. B **35**, R117 (2002).
[2] M. S. Pindzola and F. Robicheaux, Phys. Rev. A **54**, 2142 (1996).
[3] K. Bartschat and I. Bray, J. Phys. B **29**, L577 (1996).
[4] M. Baertschy, T. N. Rescigno, W. A. Isaacs, X. Li, and C. W. McCurdy, Phys. Rev. A **63**, 022712 (2001).
[5] J. Colgan, M. Pindzola, and F. Robicheaux, J. Phys. B **34**, L457 (2001).
[6] C. W. McCurdy, D. A. Horner, T. N. Rescigno, and F. Martín, Phys. Rev. A **69**, 032707 (2004).
[7] J. Colgan and M. S. Pindzola, Phys. Rev. A **65**, 022709 (2002).
[8] D. C. Griffin, M. S. Pindzola, C. P. Ballance, and J. Colgan, Phys. Rev. A **79**, 023413 (2009).
[9] W. Vanroose, F. Martín, T. N. Rescigno, and C. W. McCurdy, Phys. Rev. A **70**, 050703(R) (2004).
[10] J. Colgan, M. S. Pindzola, and F. Robicheaux, Phys. Rev. Lett. **98**, 153001 (2007).
[11] J. Colgan, M. S. Pindzola, and F. Robicheaux, Phys. Rev. Lett. **93**, 053201 (2004).
[12] M.-T. Huang, R. Wehlitz, Y. Azuma, L. Pibida, I. A. Sellin, J. W. Cooper, M. Koide, H. Ishijima, and T. Nagata, Phys. Rev. A **59**, 3397 (1999).
[13] R. Wehlitz, M. M. Martinez, J. B. Bluett, D. Lukic, and S. B. Whitfield, Phys. Rev. A **69**, 062709 (2004).
[14] R. Wehlitz, J. Colgan, M. Martinez, J. Bluett, D. Lukic, and S. Whitfield, J. Electron Spectrosc. Relat. Phenom. **144-147**, 59 (2005).
[15] J. Colgan, D. C. Griffin, C. P. Ballance, and M. S. Pindzola, following paper, Phys. Rev. A **80**, 063414 (2009).
[16] A. S. Kheifets and I. Bray, Phys. Rev. A **58**, 4501 (1998).
[17] A. S. Kheifets and I. Bray, Phys. Rev. A **75**, 042703 (2007).
[18] A. S. Kheifets, I. Bray, and J. Hoszowska, Phys. Rev. A **79**, 042504 (2009).
[19] A. S. Kheifets, Phys. Rev. A **71**, 022704 (2005).
[20] I. Bray and A. T. Stelbovics, Phys. Rev. Lett. **70**, 746 (1993).
[21] I. Bray and D. V. Fursa, Phys. Rev. A **54**, 2991 (1996).
[22] A. Borovik, A. Muller, S. Schippers, I. Bray, and D. V. Fursa, J. Phys. B **42**, 025203 (2009).
[23] L. Vo Ky, P. Faucher, A. Hibbert, J.-M. Li, Y.-Z. Qu, J. Yan, J. C. Chang, and F. Bely-Dubau, Phys. Rev. A **57**, 1045 (1998).
[24] T. A. Ferrett, D. W. Lindle, P. A. Heimann, W. D. Brewer, U. Becker, H. G. Kerkhoff, and D. A. Shirley, Phys. Rev. A **36**, 3172 (1987).
[25] R. Wehlitz, J. B. Bluett, and S. B. Whitfield, Phys. Rev. Lett. **89**, 093002 (2002).
[26] R. Wehlitz, J. B. Bluett, and S. B. Whitfield, Phys. Rev. A **66**,

012701 (2002).
[27] L. Vo Ky, P. Faucher, H. L. Zhou, A. Hibbert, Y.-Z. Qu, J.-M. Li, and F. Bely-Dubau, Phys. Rev. A **58**, 3688 (1998).
[28] A. S. Kheifets and I. Bray, Phys. Rev. A **57**, 2590 (1998).
[29] Z.-C. Yan, Phys. Rev. A **60**, R3358 (1999).
[30] Y. Ralchenko, A. Kramida, J. Reader, and NIST ASD Team, *NIST Atomic Spectra Database*, 3rd ed. (National Institute of Standards and Technology, Gaithersburg, MD, 2008), http://physics.nist.gov/asd3
[31] D. A. Varshalovich, A. N. Moskalev, and V. K. Khersonskii, *Quantum Theory of Angular Momentum*, 1st ed. (World Scientific, Philadelphia, 1988).
[32] D. V. Fursa and I. Bray, Phys. Rev. A **52**, 1279 (1995).
[33] M. Y. Amusia, *Atomic Photoeffect* (Plenum Press, New York, 1990).
[34] J. McGuire, *Electron Correlation and Dynamics in Atomic Collisions*, Cambridge Monographs on Atomic, Molecular and Chemical Physics Vol. 8 (Cambridge University Press, Cambridge, 1997).
[35] A. Knapp *et al.*, Phys. Rev. Lett. **89**, 033004 (2002).
[36] G. Mehlman, J. W. Cooper, and E. B. Saloman, Phys. Rev. A **25**, 2113 (1982).
[37] R. Wehlitz (private communication).
[38] J. A. R. Samson, W. C. Stolte, Z. X. He, J. N. Cutler, Y. Lu, and R. J. Bartlett, Phys. Rev. A **57**, 1906 (1998).
[39] J. Colgan, M. S. Pindzola, and F. Robicheaux, Phys. Rev. A **72**, 022727 (2005).
[40] G. Zhu, M. Schuricke, J. Steinmann, J. Albrecht, J. Ullrich, I. Ben-Itzhak, T. J. M. Zouros, J. Colgan, M. S. Pindzola, and A. Dorn, Phys. Rev. Lett. **103**, 103008 (2009).
[41] A. S. Kheifets, I. Bray, and K. Bartschat, J. Phys. B **32**, L433 (1999).
[42] A. S. Kheifets, Phys. Rev. A **69**, 032712 (2004).
[43] A. S. Kheifets, J. Phys. B **26**, 2053 (1993).